

# Final CRADA Report – NFE-21-08693



R. H. Goulding  
R. M. Magee  
And the ORNL and TAE Teams

**April 2024**



## DOCUMENT AVAILABILITY

**Online Access:** US Department of Energy (DOE) reports produced after 1991 and a growing number of pre-1991 documents are available free via <https://www.osti.gov>.

The public may also search the National Technical Information Service's [National Technical Reports Library \(NTRL\)](#) for reports not available in digital format.

DOE and DOE contractors should contact DOE's Office of Scientific and Technical Information (OSTI) for reports not currently available in digital format:

US Department of Energy  
Office of Scientific and Technical Information  
PO Box 62  
Oak Ridge, TN 37831-0062  
**Telephone:** (865) 576-8401  
**Fax:** (865) 576-5728  
**Email:** [reports@osti.gov](mailto:reports@osti.gov)  
**Website:** [www.osti.gov](http://www.osti.gov)

This report was prepared as an account of work sponsored by an agency of the United States Government. Neither the United States Government nor any agency thereof, nor any of their employees, makes any warranty, express or implied, or assumes any legal liability or responsibility for the accuracy, completeness, or usefulness of any information, apparatus, product, or process disclosed, or represents that its use would not infringe privately owned rights. Reference herein to any specific commercial product, process, or service by trade name, trademark, manufacturer, or otherwise, does not necessarily constitute or imply its endorsement, recommendation, or favoring by the United States Government or any agency thereof. The views and opinions of authors expressed herein do not necessarily state or reflect those of the United States Government or any agency thereof.

**FINAL CRADA REPORT NFE-21-08693**

R. H. Goulding  
R. M. Magee  
And the ORNL and TAE Teams

April 2024

Prepared by  
OAK RIDGE NATIONAL LABORATORY  
Oak Ridge, TN 37831  
managed by  
UT-BATTELLE LLC  
for the  
US DEPARTMENT OF ENERGY  
under contract DE-AC05-00OR22725



## CONTENTS

CONTENTS .....	iii
ABSTRACT.....	1
1. STATEMENT OF OBJECTIVES .....	1
2. BENEFITS TO THE FUNDING DOE OFFICE’S MISSION.....	2
3. TECHNICAL DISCUSSION OF WORK PERFORMED BY ALL PARTIES .....	2
3.1 ELECTRICAL DESIGN.....	3
3.1.1 Antenna.....	3
3.1.2 Matchboxes and decoupler .....	12
3.2 MECHANICAL DESIGN (TAE TEAM).....	20
4. COMMERCIALIZATION POSSIBILITIES .....	22
5. PLANS FOR FUTURE COLLABORATION .....	23
6. CONCLUSION.....	23
REFERENCES.....	23

## ABSTRACT

TAE Technologies is developing a magnetic fusion energy concept known as the beam-driven field-reversed configuration (FRC) [1,2,3] with the ultimate goal of developing a reactor for commercial electricity production capable of burning aneutronic pB11 fuel [4]. To achieve the high plasma temperatures this requires, auxiliary radiofrequency (RF) heating will likely be needed. High Harmonic Fast Wave (HHFW) heating has been identified as a candidate RF heating scheme to overcome the unique challenges posed to RF heating by the FRC, including the large distance from the plasma edge to the last closed flux surface and a magnetic field profile with strength decreasing from edge to core and reversing sign at a null point inside the plasma.

The purpose of this project was to develop the experimental capabilities to test HHFW on TAE's C-2W device through the design of a phased array antenna and accompanying matching network. The design was performed by ORNL and informed by experiments with a prototype four-strap phased antenna-array that was manufactured and installed on the LArge Plasma Device (LAPD) at UCLA and simulations conducted with the Petra-M code under the purview of a previous INFUSE grant. The ORNL team completed the conceptual design of the antenna and matching network which was then handed off to the TAE Mechanical Design team. The design was then iterated on to ensure changes to the mechanical design did not interfere with the RF performance. This process is now complete, and, with mechanical design in hand, TAE is proceeding with plans for final integration.

### 1. STATEMENT OF OBJECTIVES

The completion of this project represents a significant step forward for TAE's RF Program, advancing it along the roadmap to high power RF injection for core plasma heating in our next generation FRC. The foundational work this project is built upon is important, including low power experiments in the LAPD [5] and simulations of HHFW in the FRC with Petra-M [6], but until a proof-of-concept system is deployed and its utility on a high performance FRC demonstrated, the HHFW-FRC pairing remains unproven. The objective of this project was to put TAE in the position to deploy such a system.

The Tasks are laid out in the proposal are repeated in the table below, along with approximate completion date.

Task Objective	Milestones	Deliverable
Develop high power antenna concept	Contractor will review results of previous work on plasma coupling	Concept model for high power HHFW launcher
	Contractor and Participant will develop antenna concept including strap arrangement, enclosure configuration, and overall dimensions	
Design feed and matching network	Contractor will develop models for hybrid and conjugate-tee based feed and matching systems using FDAC or other RF network modeling software	Feed and matching system layout and component values
	Contractor will compare performance of both models to determine which configuration is most suitable for application on C-2W. The model will then be used to determine suitable values for actuators such as tuning capacitors	

Produce mechanical design of high power HHFW launcher	Contractor and Participant will create mechanical design of launcher at level of preliminary design	Model and drawing set at preliminary design level
Contractor and Participant will complete CRADA final report		This report

## 2. BENEFITS TO THE FUNDING DOE OFFICE'S MISSION

This project advances the mission of the DoE Office of Science Fusion energy program by building knowledge in the general areas of alternative magnetic confinement and RF heating of plasmas, in addition to the specific areas of application.

The need for research into tokamak alternatives to hedge the fusion energy bet, to expand experimental parameter space to stress test models and understanding, and to push the bounds on the development of actuators has been articulated elsewhere [7,8]. The FRC is an attractive alternative to the tokamak for several well-publicized reasons, including engineering simplicity, a natural, expandable divertor, demonstrated non-inductive sustainment, and, most significantly, minimal magnetic field requirements which obviate the need for superconductors and enables the use of advanced fuels. Despite these advantages, the FRC is less well-developed as a fusion concept than the tokamak or stellarator. Funding of this project has in a small yet meaningful contribute to restoring balance.

An example of a specific area of interest to the general fusion community is the interaction of RF waves with fast ions. As tokamaks move into the burning plasma era, the interaction of RF waves with large populations of fusion alphas will become a major focus of research. RF has the potential to improve fusion energy capture via alpha channeling [9], mitigate the effects of fast ion driven instabilities [10], and accelerate beam-injected ions to high energies more efficiently than electrostatic acceleration [11]. RF heating schemes will also increasingly need to deal with the practical challenges of coupling to the thermal plasmas in the presence of large non-thermal populations. Because TAE's beam-driven FRCs naturally support a large population of fast ions, this proposal has enabled the RF-fast ion interaction to be studied experimentally in advance of the ITER-era.

More directly, this research will impact all of those devices employing HHFW. The most notable being the spherical tokamak NSTX. A major result from that experimental program is that edge density fluctuations with a filamentary structure can significantly sap injected power [12,13]. Perhaps the unique injection geometry in the FRC will provide insight into rectifying this long-standing problem.

Finally, if HHFW can be shown to efficiently couple power to the FRC plasma core, it can open the door for research into advanced fuels, such as p-B11. The potential advantages of a fusion reactor operated on p-B11 fuel are widely agreed upon, but so too are the physics challenges remaining to develop such a reactor. This proposal will advance development of solutions to that challenge.

## 3. TECHNICAL DISCUSSION OF WORK PERFORMED BY ALL PARTIES

All four of the task laid out in the Scope of Work have now been completed. The conceptual design of the antenna (Task 1) and the Design of the Matching Network (Task 2) were completed by Richard Goulding at ORNL. The conceptual design was then handed off to the TAE Mechanical Design Team led by Jon Schroeder. The mechanical design of the antenna was then produced through an iterative process between TAE and ORNL. Weekly meetings were held to ensure that the mechanical design decisions made by the TAE team did not interfere with the RF Engineering requirements. Once the design was

complete, it was again analyzed from the RF perspective by the ORNL team and given the stamp of approval (Task 3). The drafting of this report represents the completion of the final task (Task 4).

### 3.1 ELECTRICAL DESIGN

The electrical design was performed by producing first a conceptual 3-D model in COMSOL. The plasma is modeled as a lossy dielectric load to reduce calculation time. Then a mechanical model was produced based on this electrical design, and in turn a more accurate electrical model was produced based on the mechanical design. The final model includes the complete antenna structure, the inner wall of the vacuum vessel, and the port wall and flange. The decision was made during the design activity to have a separate RF source for each current strap. As a result, it was decided to not include a load resilient circuit, which could only have one power source for each azimuthal strap pair and would significantly increase the size, cost, and complexity of the circuit. Table 1. provides the basic parameters used in the electrical design:

**Table 1. Basic design parameters**

Parameter	Value
Number of current straps	4
Number of RF sources	4
Input power	25 kW/line
Operating frequencies	13.56 MHz or 27 MHz

An important feature that was retained was the use of decouplers connected between axial current strap pairs. This allows arbitrary axial phasing with equal currents on the current straps for equal input powers from the sources. It also greatly reduces interactions between tuning elements for the matching network for each current strap. This is discussed below.

The COMSOL model was used to model voltages, electric fields and current distributions throughout the antenna. An assumed resistive loading was used to scale the antenna current in the COMSOL model to a value consistent with the forward power specified in order to estimate electric fields and voltages. COMSOL was also used to calculate scattering parameters for use in design of the matching/decoupling network. Details of this work are described below.

#### 3.1.1 Antenna

##### 3.1.1.1 Basic Geometry

The first step was to select a basic geometry for the antenna. This was done by creating fully parameterized 3-D models in COMSOL for different configurations. Figure 1 shows geometries examined including 2 axial x 2 azimuthal end and center grounded types, and 4 axial x 1 azimuthal layouts. The last of these was ruled out by the need to have a retractable antenna.

The remaining options were first compared by estimating plasma coupling. The estimate was made by using COMSOL to calculate values for the RF magnetic field strength ( $\vec{B}$ ) near the front surface of the straps along an azimuthal path. Figure 2a shows the paths over which the values are graphed (magneta curves) while Figure 2b shows the results. The plasma resistive coupling  $R$  is roughly proportional to  $\int |\vec{B}_{||}|^2 ds$ , so that integrating under the curves in Figure 2b gives relative values of  $R$ . Then, the current needed to couple the same amount of power for each configuration can be determined simply using  $P = I^2 R$ . The currents were used to scale the COMSOL results and calculate the maximum value of the



electric field  $E_{\max}$  for each configuration. This was found to be slightly higher ( $\sim 6\%$ ) for the center grounded configuration than for the end grounded. In the case that  $E_{\max}$  is the power limiting factor, this translates to 12% more power, so the end grounded design was selected.

The available ports are canted such that the axis of the port does not pass through the machine axis but intersects the vertical line passing through the machine axis at the “impact parameter” ( $I_p$ ), as illustrated in Figure 3. To maximize coupling, all portions of the current straps should be at fixed radii relative to the machine axis. This can be done by producing asymmetric upper and lower antenna sections (red lines in Figure 3). Formulas were developed to create strap models that meet this requirement, with parameters that can be varied such as the strap inner radius, total box height, and gaps between the straps and the horizontal septa.

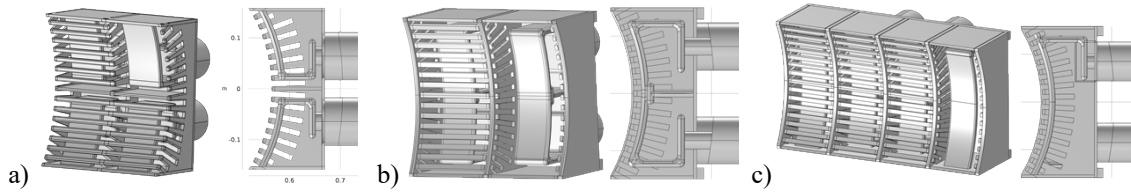


**Figure 1. Original antenna concepts a) End grounded, b) Center grounded, c) 4 axial straps**

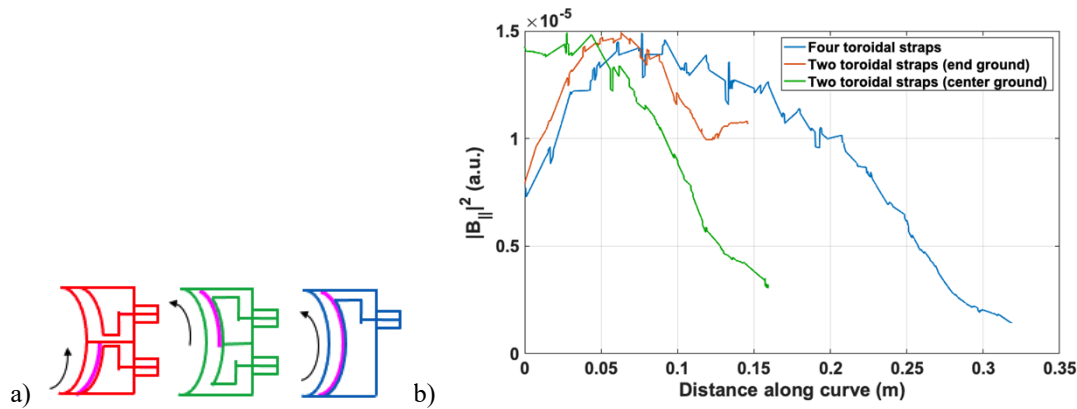


**Figure 2. a) measurement paths (magenta lines) for end grounded, center grounded, and four-strap antennas, b) graphs of  $|\vec{B}_{\parallel}|^2$  along curves shown in a)**

The parametrized COMSOL model produced in this way was used by TAE to produce the mechanical model that was then provided to ORNL in turn for final modeling of the electrical characteristics. To avoid meshing errors, a new model was built in COMSOL over the imported mechanical model produced by TAE.

Reproduction of RF-relevant features of the mechanical model can be seen in views of the final COMSOL model shown in Figure 4. One such feature that can be seen in the figure is slotted vertical septa, that reduce mutual coupling between horizontally adjacent straps, but that have reduced image currents for improvement of the  $k_{\parallel}$  spectrum. Horizontal septa separate vertically adjacent straps. These are solid, and, as a result, the mutual coupling between such strap pairs and between diagonally adjacent pairs is small. Another feature of the design is the use of boron nitride sidewalls outside the outer vertical septa. Note: the electrical model does not include the radiusing applied to all sharp edges found in the mechanical model.

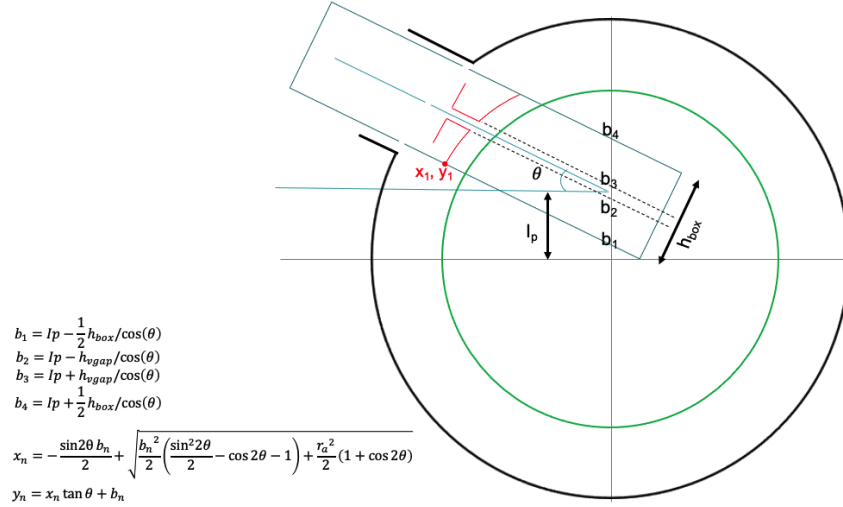


**Figure 3. Schematic geometry for asymmetric straps (red) having constant gap to cylindrical plasma (green circle). The formulas give  $x_n, y_n$ , the four endpoints for the two straps with a constant radius  $r_a$ .  $h_{vgap}$  is twice the length of a perpendicular between the two dashed lines.**

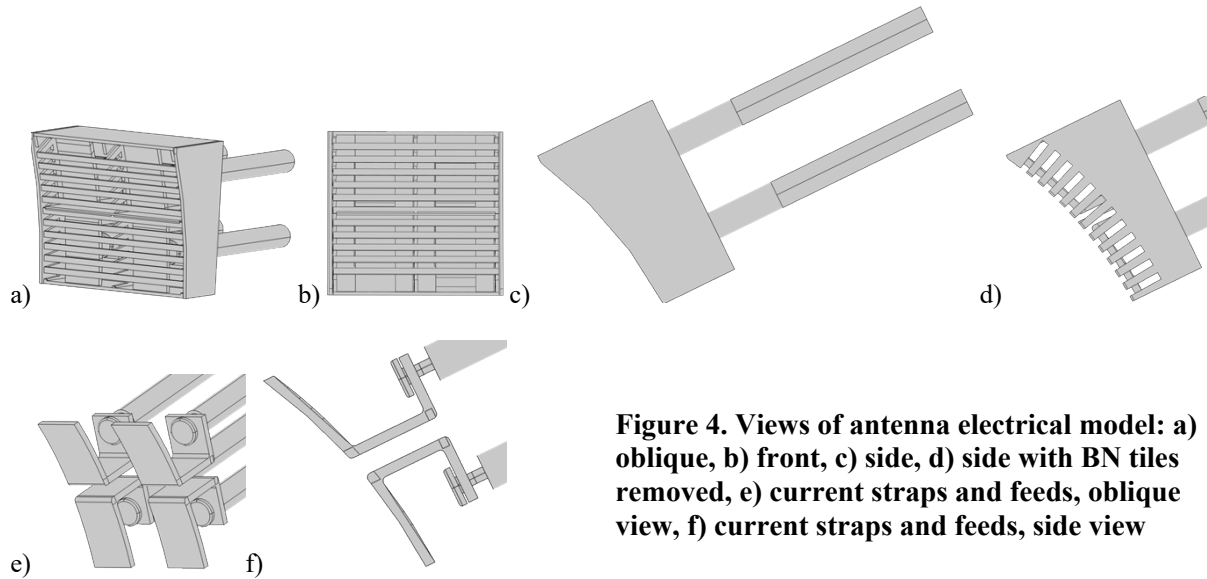


**Figure 4. Views of antenna electrical model: a) oblique, b) front, c) side, d) side with BN tiles removed, e) current straps and feeds, oblique view, f) current straps and feeds, side view**

### 3.1.1.2 Magnetic field profile and vacuum spectrum

RF magnetic field profiles were calculated along a constant radius curve located in front of and centered on each vertical pair of current straps. The strap numbering is shown in Figure 5. Figure 6 shows a comparison of  $|\vec{B}_{\parallel}|^2$  for the different vertical pairs, at both 13.56 MHz and 27 MHz. The inset in the lower right of the figure shows the antenna and the curve for which  $|\vec{B}_{\parallel}|^2$  is plotted. The zero-distance location on the curve and direction of increasing distance is shown by the arrow. There is an  $\sim 20\%$  difference in the peak values for the two straps, with the lower peak corresponding to the upper strap with the peak centered at a “distance along curve” of  $\sim 0.4\text{m}$ . The current magnitudes are the same at the strap

grounds, so that it would be expected to have higher coupling for that strap, since the box is deeper, and the return strap is further away from the radiating current strap. Some of the asymmetry may be due to the increased gap between the strap and the measurement location for the upper strap. Finally, it can be seen that the left and right vertical strap pairs are nearly identical, and also that there is little increased drop-off due to finite wavelength effects as the distance from the grounded ends increases for the higher frequency in comparison to the lower one.

Another antenna related modeling outcome is with regards to the launched  $k_{\parallel}$  spectrum. The spectrum was found to be influenced significantly by the presence of the metal sidewalls. A comparison was made with and without them included as shown in the two antenna models in Figure 7. They are used to help provide rigidity to the antenna box so that their removal was done just as a modeling exercise. Figure 8 shows the line over which  $\tilde{B}_{\parallel}$  data was obtained from the model.

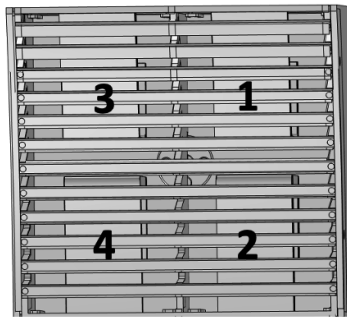


Figure 5. Strap numbering

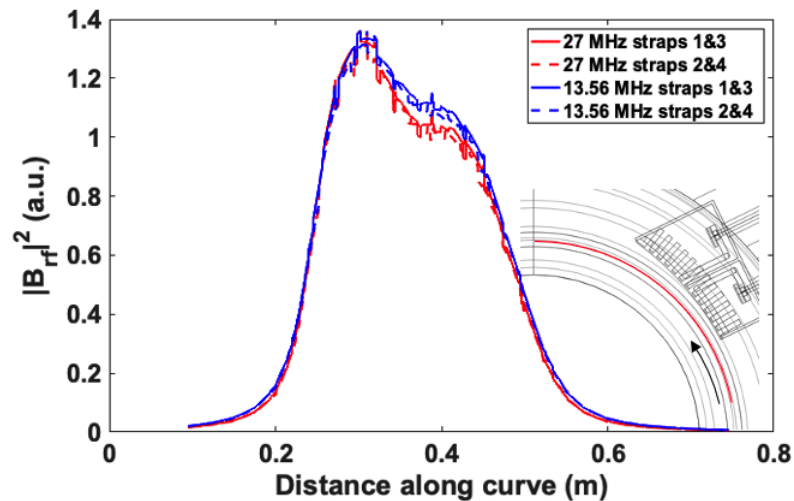
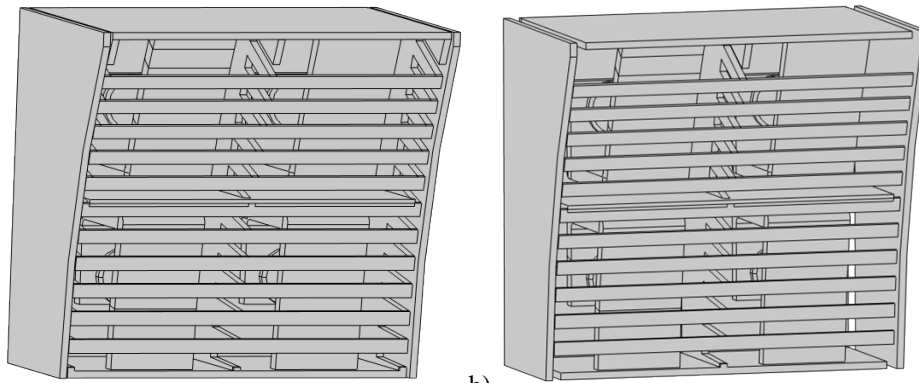
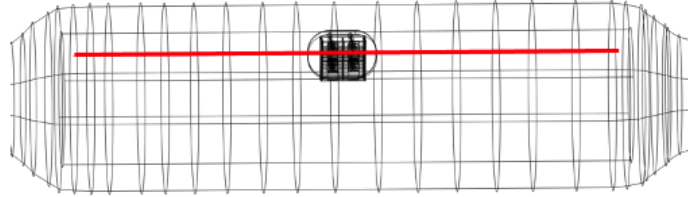


Figure 6.  $\tilde{B}_{\parallel}$  profiles for vertical strap pairs, 13.56 MHz and 27 MHz



a) and b) Antennas with a), and without b) sidewalls on left and right-hand sides



**Figure 8. Line over which  $\tilde{B}_{\parallel}$  is measured for spectral analysis. Line is  $\sim 7$  cm in front of current strap**

The resulting  $\tilde{B}_{\parallel}$  magnitudes and phases are shown in Figures 9 a and b, for relative strap phasing between axially adjacent straps of  $0^{\circ}$ . It is seen from the figures that the metal sidewalls have little influence on the phase of  $\tilde{B}_{\parallel}$ , but the magnitudes of the return currents are significantly higher when they are present, despite the fact that they are slotted. This results in a shift of the first peak in the  $k_{\parallel}$  spectrum to higher values, as shown in Figure 10. The effect of axial phasing on the spectra on the current magnitude and phase are shown in Figures 11 a and b, while the effect on the  $k_{\parallel}$  spectrum is shown in Figure 12. The cases shown in these figures all include metal sidewalls.

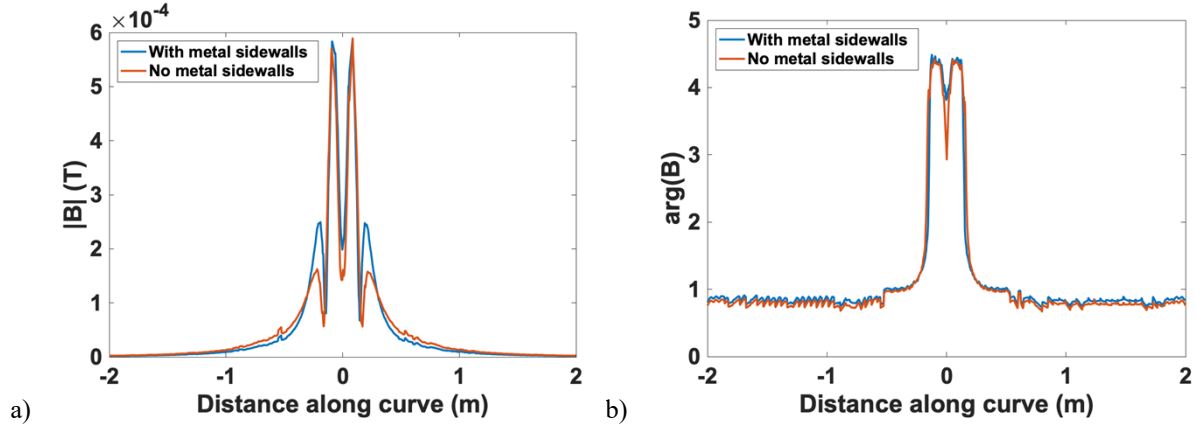


**Figure 9. Profiles of  $\tilde{B}_{\parallel}$  a) magnitude, and b) phase, for boxes with and without metal sidewalls.**

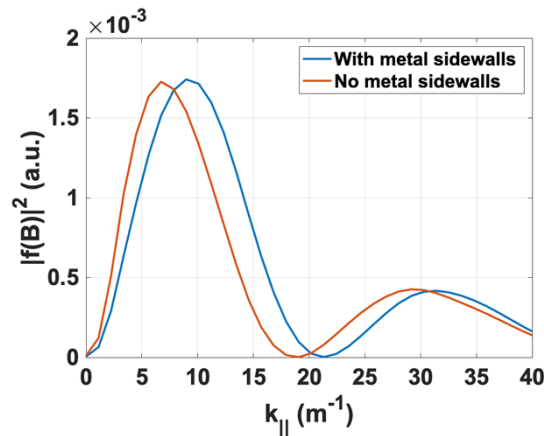


**Figure 10. Comparison of  $k_{\parallel}$  spectra for antenna boxes with and without metal sidewalls**

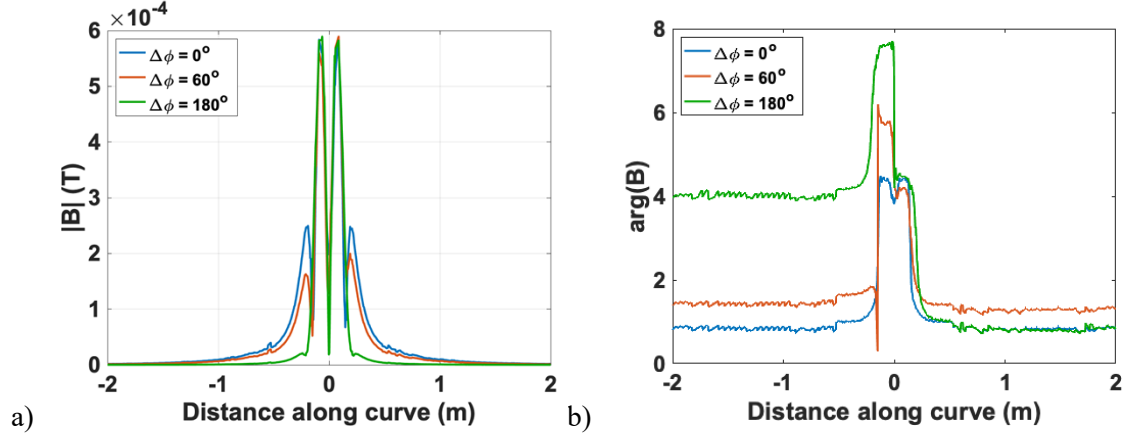


**Figure 11. Profiles of  $\tilde{B}_{\parallel}$  a) magnitude, and b) phase, for differing values of phasing between axially adjacent straps. In all cases the antenna box has metal sidewalls present.**

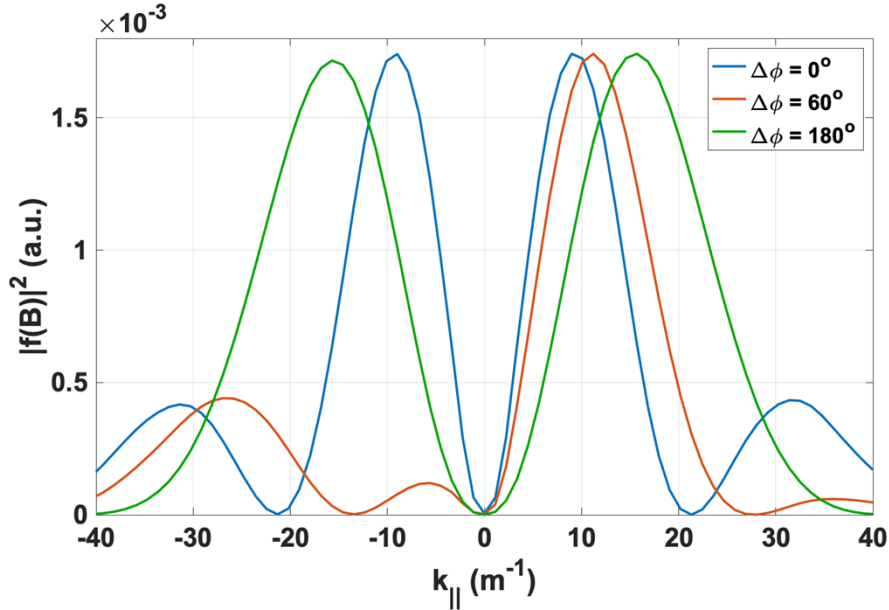


**Figure 12.  $k_{\parallel}$  spectra for phasing cases shown in Figure 11. The entire spectrum is shown to illustrate the directivity for asymmetric phasing ( $\Delta\phi = 60^\circ$ )**

It is seen from figures 10 and 12 that even for a relative phasing of  $0^\circ$  the peak in  $k_{\parallel}$  is fairly high:  $\sim 7\text{m}^{-1}$  without metal sidewalls and  $\sim 9\text{m}^{-1}$  with them. This corresponds in turn to a high parallel index of refraction. For the latter case we have  $n_{\parallel} \sim 32$  at 13.56 MHz and  $n_{\parallel} \sim 16$  at 27 MHz. The only available geometric variation that could affect this is the width of the current straps. It was found to have a very minor effect. Another possibility may be to remove the central vertical septum, but this would result in higher circulating power through the decoupler networks and higher sensitivity to the decoupler spectrum. A larger separation between straps would be effective but would result in a box too large to fit through the port.

### 3.1.1.3 Electric field magnitudes and currents

The model was used to calculate electric field values in the structure. The magnitude of  $|E|$  was determined by performing a calculation with a nominal 1 W/port forward power at the input and multiplying the resulting fields calculated by a scale factor  $S$  given by the equation,

$$S = \frac{I_P}{I_{1W}} = \sqrt{\frac{2P}{R_c}} \quad (1)$$

Where  $I_{1W(P)}$  is the current near the strap ground for a power of 1W ( $P$ ),  $P$  is the net power (in this case,  $P = 25$  kW), and  $R_c$  is the equivalent resistance at the strap ground. A conservative value of  $R_c = 0.35 \Omega$  was chosen for the calculation. The strap current  $I_{1W}$  is calculated by performing the integration  $I = \oint H_T \cdot dl$  over a path around the circumference of the current strap near where it attaches to the box, where  $H_T$  is the tangential magnetic field. The scale factors calculated are nearly the same for each strap.

The resulting electric field profiles are shown in Figures 13 a,b, and c for 13.56 MHz, and Figure 14 for 27 MHz. The maximum value for  $|E|$  in the simulation occurs at the ends of the transmission lines as can be seen from Figures 13a and 14. The maximum value of  $|E|$  calculated at 13.56 MHz is low,  $< 1$  MV/mm = 1 kV/mm. Since the model has sharp edges, it is especially conservative. The peaking for instance seen near the 90 degree bend in the strap feeds in Figure 13c is likely higher than it would be with accurate radiusing applied. The higher voltages produced at 27 MHz result in higher electric field values. The maximum observed of  $\sim 1.6$  kV/mm is not likely to cause arcing.

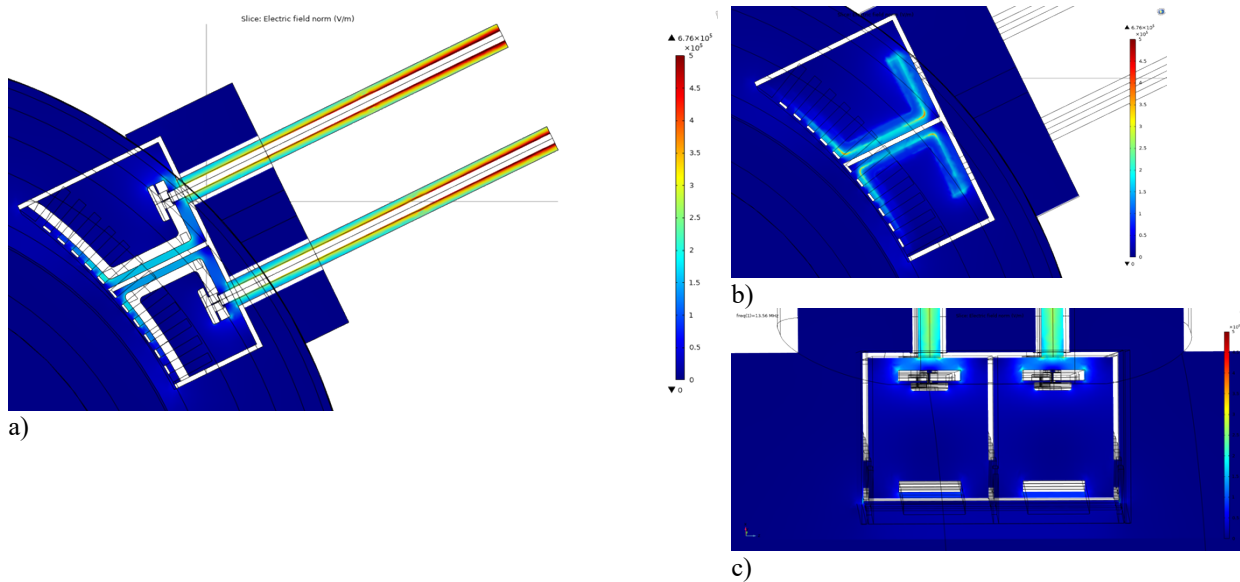


**Figure 13. a) side view of  $|E|$  for  $f = 13.56$  MHz,  $R_c = 0.35 \Omega$  showing slice in plane cutting through the center of the coax. b) side view showing slice at edge of current straps, c) top view**

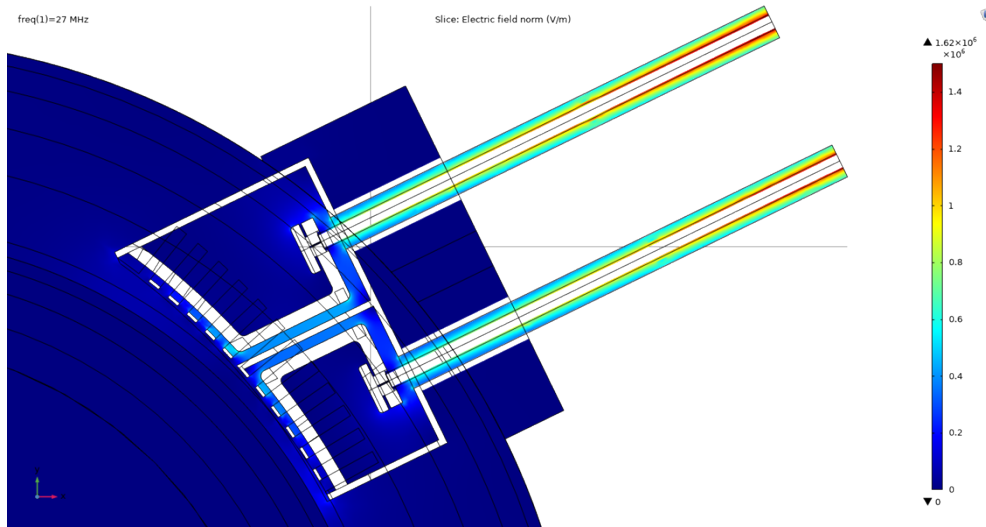


Figure 14. Side view of  $|E|$  at same location as Figure 13a, for  $f=27$  MHz,  $R_c = 0.35 \Omega$ .

In Figure 15, the white arrows show the paths of the currents while the surface color shows the current density for  $f=13.56$  MHz. It can be seen from the current direction in the feed lines that the top and bottom current straps are fed out-of-phase. This produces the desired unidirectional current paths on the strap surfaces.

We did not examine RF heating directly, but due to the relatively low power, short pulse length, and small duty factor, the temperature excursion should be limited even for high currents.

Finally, the feedthrough was modified from a design used at ORNL to provide short pulse operation at up to 30 kW. A cutaway view of the ORNL design is shown in Figure 16. Based on the voltage calculated at 27 MHz corresponding to the case shown in Figure 14, the maximum  $|E|$  value in the feedthrough is  $\sim 1.8$  kV/mm, which is also acceptable.

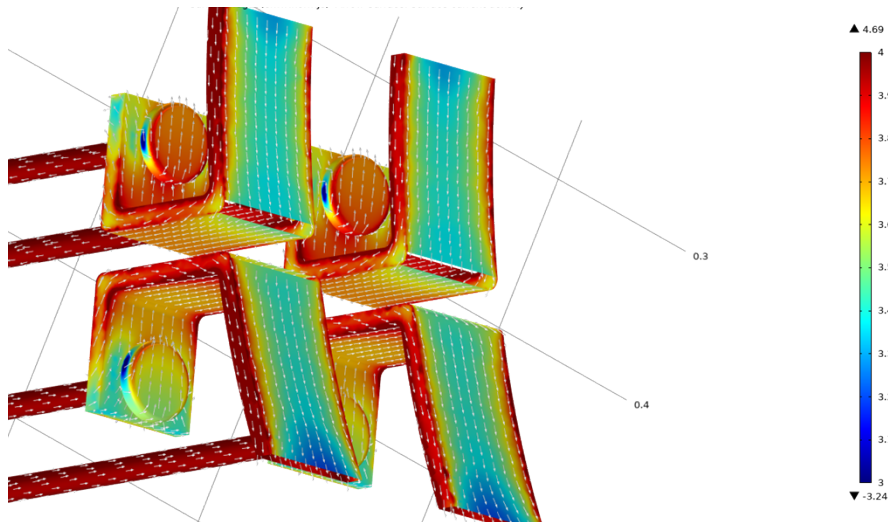
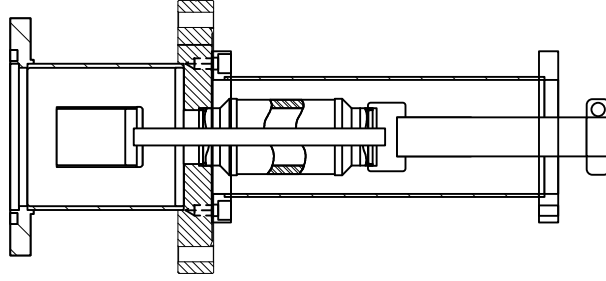
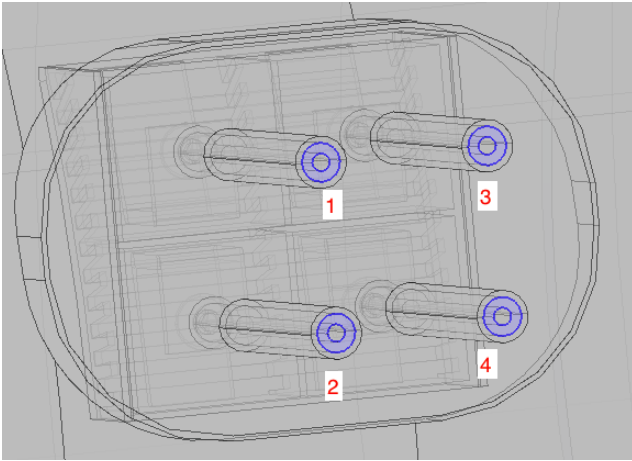


Figure 15. Current paths (white arrows) and  $\log_{10}$  of the surface current density in A/m.



**Figure 16. ORNL 30 kW feedthrough design that TAE feedthrough will be based on.**

### 3.1.1.4 Scattering Parameters and Impedance Parameters



**Figure 17. Port numbering for scattering parameters**

The four-port scattering parameters for 13.56 MHz are provided in Table 2. The parameters are defined at the port locations shown in Figure 17. The corresponding imaginary part of the impedance parameters, which are useful for determining mutual inductances, are provided in Table 3. The scattering and impedance parameters for 27 MHz are provided in Table 4 and Table 5 respectively. The impedance parameter off diagonal elements indicate fairly strong coupling ( $\sim 6\%$  ratio of mutual to self inductance) between axially adjacent straps (e.g.,  $X_{31}$ ), but are much smaller ( $\sim 1.5\%$ ) between azimuthally adjacent straps (e.g.,  $X_{21}$ ), and are very small between diagonally

adjacent straps (e.g.,  $X_{41}$ ). The scattering parameters were used for the circuit calculations described in the next section.

**Table 2. Scattering matrix for  $f = 13.56$  MHz**

$-0.8634 + 0.4966i$	$-0.0028 - 0.0069i$	$0.0155 + 0.0293i$	$-0.0006 - 0.0004i$
$-0.0028 - 0.0069i$	$-0.8796 + 0.4658i$	$-0.0006 - 0.0004i$	$0.0118 + 0.0259i$
$0.0155 + 0.0293i$	$-0.0006 - 0.0004i$	$-0.8635 + 0.4965i$	$-0.0028 - 0.0068i$
$-0.0006 - 0.0004i$	$0.0118 + 0.0259i$	$-0.0028 - 0.0068i$	$-0.8797 + 0.4655i$

**Table 3. Imaginary part of impedance matrix for  $f = 13.56$  MHz.**

13.3567	-0.1976	0.8910	-0.0179
-0.1976	12.4226	-0.0179	0.7575
0.8910	-0.0179	13.3531	-0.1964
-0.0179	0.7575	-0.1964	12.4158

**Table 4. Scattering matrix for  $f = 27$  MHz**

$-0.5007 + 0.8555i$	$-0.0121 - 0.0092i$	$0.0581 + 0.0367i$	$-0.0014 + 0.0005i$
---------------------	---------------------	--------------------	---------------------



-0.0121 - 0.0092i -0.5595 + 0.8163i -0.0014 + 0.0005i 0.0474 + 0.0368i  
 0.0581 + 0.0367i -0.0014 + 0.0005i -0.5009 + 0.8553i -0.0121 - 0.0091i  
 -0.0014 + 0.0005i 0.0474 + 0.0368i -0.0121 - 0.0091i -0.5599 + 0.8160i

**Table 5. Imaginary part of impedance matrix for f = 27 MHz**

28.7125 -0.5012 2.2985 -0.0457  
 -0.5012 26.3719 -0.0456 1.9322  
 2.2985 -0.0456 28.7019 -0.4982  
 -0.0457 1.9322 -0.4982 26.3561

### 3.1.2 Matchboxes and decoupler

The scattering parameters from the previous section were used to design the matching and decoupling networks for the antenna. A design was found that could be used at both 13.56 MHz and 27 MHz, although a slight change to smaller inductors in the decoupler circuit, to be described, are needed at the later frequency.

Figure 18 shows schematically the impedance matching circuits for a pair of axially adjacent straps. Each is connected to an identical L-network with a decoupling network in between connecting between the feedlines as shown. Both matching networks and the decoupler circuit are included in the same enclosure. In the schematic X1 and X2 are the transmitters for the two ports, C1 and C3 are identical series capacitors and C2 and C4 are identical shunt capacitors. L1 and L2 are identical inductors whose purpose is to lower the required capacitance of C2 and C4 which otherwise would be > 1000 pF at 13.56 MHz. At 27 MHz, these inductors are eliminated; the inductance of the connecting lines are sufficient to provide the needed inductance in that case.

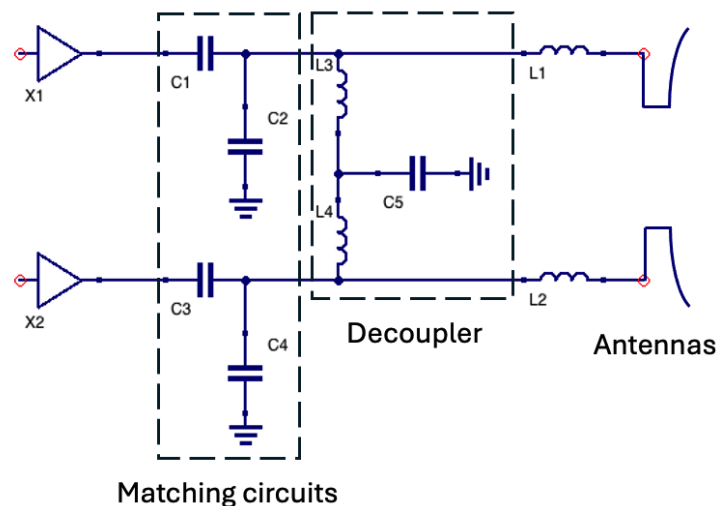


**Figure 18. Schematic of matching and decoupler network feeding two axially adjacent current straps from two transmitters X1 and X2.**

The decoupler network consists of two identical inductors L3 and L4 and the capacitor C5 which provides an adjustable amount of power flow between the circuits to compensate for that occurring due to the antenna mutual inductances. The connections between the two outputs of the decoupler and the antennas is 3-1/8" hardline. The connections between the transmitters and the two inputs to the matching circuits

can be any type of heliax rated for 25 kW average power at 27 MHz. Indeed, due to the short pulse length, and the fact that the transmitter likely cannot run full power at VSWR > 2, any cable rated for 50 kW peak power would suffice, even if the average power rating is substantially less than 25 kW.

Table 6 shows the vacuum capacitors and inductor component values that are recommended for this circuit.

**Table 6. Circuit components for two-strap matching and decoupling network**

Circuit designation	Description	Component value	Type
C1, C3	Series capacitor, matching network	10-75 pF	Comet CVNA-75AC/60
C2, C4	Shunt capacitor, matching network	15-250 pF	Comet CVSA-250AC/40
L1, L2	Inductor, matching network (13.56 MHz operation only)	233 nH	N/A
C5	Capacitor, decoupling network	100-1000 pF	Comet CVUN-1000CC/10
L3, L4	Inductor, decoupling network (13.56 MHz)	3000 nH	N/A
L3, L4	Inductor, decoupling network (27 MHz)	2000 nH	N/A

Table 7 below gives the design parameters for the inductors:

**Table 7. Design parameters for inductors L1 through L4 for 13.56 MHz and 27 MHz operation [14]**

Circuit designation	Frequency	Number of turns	Mean Diameter "D"	Inductor Length "l"	Wire diameter "d"	Pitch "p"	AC Resistance
L1, L2	13.56 MHz	5	1.12 in	2.5 in	0.258 in	0.5 in	0.029 Ω
L1, L2	27 MHz	N/A	N/A	N/A	N/A	N/A	N/A
L3, L4	13.56 MHz	11	2.2 in	3.5 in	0.162 in	0.322 in	0.22 Ω
L3, L4	27 MHz	9	2.2 in	3.5 in	0.162 in	0.394 in	0.15 Ω

Note: L1 and L2 are not used for 27 MHz operation.

A schematic explanation of the various dimensions listed in Table 6 is provided in Figure 19 below.

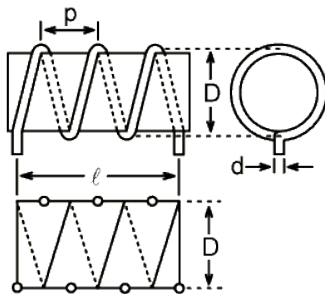


**Figure 19. Explanation of dimensions in Table 6.[14]**

Next, we discuss the method that was used to make the design choices described above. In order to define the values needed for the circuit elements it is necessary to examine the range of plasma loads that may be expected for the antenna. We take the simple approach in this calculation of varying the real part of the diagonal elements of the impedance matrix over the range of desired resistances. The new impedance matrix for a given resistance R is calculated simply as follows:

$$Z = Z_c - Z_{cr} + I * R \quad (2)$$

Where  $\mathbf{Z}_c$  is the original impedance matrix,  $\mathbf{Z}_{cr}$  is the real part of the diagonal elements of  $\mathbf{Z}_c$ ,  $\mathbf{I}$  is the identity matrix, and  $R$  is the scalar value of the resistance that is scanned over the desired range for the calculation.

In order to calculate the component values found in Figure 18 the value  $\mathbf{Z}$  must first be transformed from the reference planes of the COMSOL simulation to the locations for each pair of straps at the junctions between the main lines and L3 and L4 in the decoupler network. First  $\mathbf{Z}$  is transformed along the coaxial lines over the distance from reference planes to the matchbox. Since these lines have no coupling with each other, there is an easy transformation in matrix notation. If we designate the transformed impedance matrix as  $\mathbf{Z}'$ , then it is given by the expression:

$$\mathbf{Z}' = [\mathbf{CZ} + jZ_0\mathbf{S}] \left[ \mathbf{C} + j \frac{1}{Z_0} \mathbf{SZ} \right]^{-1}$$

Where we have the diagonal matrices

$$\mathbf{C} = \begin{pmatrix} \cos \beta l_1 & & & \\ & \cos \beta l_1 & & \\ & & \cos \beta l_1 & \\ & & & \cos \beta l_1 \end{pmatrix} \text{ and } \mathbf{S} = \begin{pmatrix} \sin \beta l_1 & & & \\ & \sin \beta l_1 & & \\ & & \sin \beta l_1 & \\ & & & \sin \beta l_1 \end{pmatrix}$$

And  $l_1$  through  $l_4$  are the lengths of the four connecting lines.

We next have the transformation due to the series inductances  $L_1$  and  $L_2$  in Figure 18. Assuming they are equal for all four lines, and equal to  $L_s$ , then at the junction of the decoupler we have,

$$\mathbf{Z}'' = \mathbf{Z}' + L_s \mathbf{I}$$

In order to include the effect of the decoupling networks, it is best to convert to an admittance matrix  $\mathbf{Y}'' = \mathbf{Z}''^{-1}$  since these are connected in parallel across line pairs. We treat the decouplers as lossless 2-port networks having the configuration shown in Figure 20. Decoupling is only done between the line pairs 1 and 3 and 2 and 4, since the strong mutual impedances exist only between these pairs. Going from the load to the generator side of the decoupling network, the admittance matrix transforms simply as

$$\mathbf{Y}''' = \mathbf{Y}'' + \mathbf{Y}_d \quad (3)$$

where  $\mathbf{Y}'''$  is the generator side admittance matrix and  $\mathbf{Y}_d$  is the admittance matrix for the decoupler networks. Then to cancel out the cross coupling between the strap pairs, we simply require  $Y_{d13} = Y_{d31} = -\text{Im}(Y''_{31})$ , and  $Y_{d24} = Y_{d42} = -\text{Im}(Y''_{42})$ . Note that the decoupling network is assumed pure imaginary, and only the imaginary part of the antenna cross coupling, which is due to the strap mutual inductances, can be cancelled out. Looking at the decoupler between straps 1 and 2 (the identical procedure is used for the other one) It can be shown that for this to happen, the value of  $X_3$  in Figure 20 is given by the equation

$$X_3 = -\frac{X^2 B}{1 + 2XB} \quad (4)$$

Where  $B = \text{Im}(Y''_{31})$  and  $X = X_1 = X_2 = \omega L_3 = \omega L_4$ , where  $\omega$  is the angular frequency and the inductances are defined in Figure 18. Determination of  $X_3$  then allows the decoupler capacitance to be calculated directly.

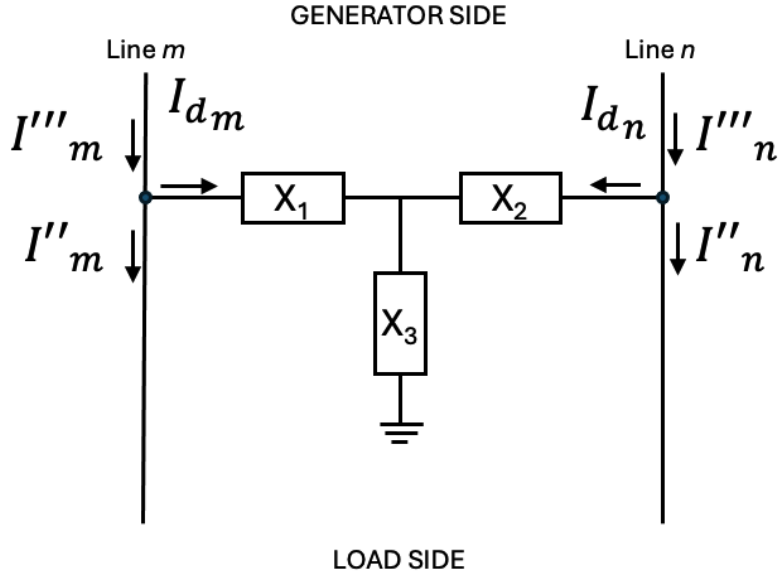


**Figure 20. Schematic of decoupling network including currents and admittances**

Finally, for this value of  $X_3$  we have additionally,

$$Y_{d11} = Y_{d33} = -j \frac{X + X_3}{X^2 + 2XX_3} \quad (5) \quad \text{and} \quad Y_{d13} = Y_{d31} = j \frac{X_3}{X^2 + 2XX_3} \quad (6)$$

Equation 3 is for the full 4 x 4 admittance matrix. The values of  $Y_{d22}$  and  $Y_{d44}$  corresponding to the other decoupler can be calculated using Eqn. 5, and  $Y_{d24}$ ,  $Y_{d42}$  can be calculated from Eqn. 6, with the understanding that in Eqn. 4 the value of  $B$  in that case is given by  $B = \text{Im}(Y''_{42})$ . The other elements in the 4 x 4 admittance matrix are all approximated as 0.

At this point,  $\mathbf{Y}_d$  is fully defined. Eqn. 3 then gives the value for the admittance matrix on the generator side of the decouplers.

While the decoupler capacitances can be calculated from the impedance matrix alone, just cancelling out  $\text{Im}(Y'_{31})$  and  $\text{Im}(Y''_{42})$ , those needed to produce an impedance match require a determination of the active impedance directly on the load side of the shunt capacitors C2 and C4 in Figure 18. Because of the cross terms in the impedance matrix, these impedances for each port depend on the currents on each of the current straps. To calculate these, we go back to the impedance matrix defined at the reference planes. In matrix notation we have:

$$\mathbf{V} = \mathbf{Z}\mathbf{I} \quad (7)$$

Where  $\mathbf{V}$  and  $\mathbf{I}$  are vectors representing the complex voltages and currents at the four ports, and  $\mathbf{Z}$  is the impedance matrix at the reference plane. Then the active impedances  $Z_a$  at each port  $n$  are simply given by the expression

$$Z_{an} = V_n/I_n = \sum_j Z_{n,j} I_j / I_n \quad (8)$$

The currents  $I_n$  are calculated based on the requirements that the forward power in each of the lines is 25 kW, and that the phases of the currents have the chosen values based on the desired  $k_{||}$  at the peak of the vacuum spectrum. It is also desirable for the currents to have as close as possible equal magnitudes because this maximizes the coupled power when all straps are operated at close to the voltage limit. The optimal location to define the magnitudes and phases of the currents are at the strap grounds since the maxima occur there. On the other hand, the impedance matrix is defined for the reference planes shown in Figure 17. We do not know directly what the relation is between currents at the strap grounds is to those at the reference planes, but we do know that unless the VSWR is very low in some lines the complex ratios of the currents at the strap grounds should be close to those of the voltages at the voltage maxima in the transmission lines, which we can calculate from values found at the reference planes. The procedure is as follows:

1. A current vector is formed having the desired phases and equal magnitudes
2. The active impedances are calculated using Eqn. 8 and the complex reflection coefficients  $\Gamma_n$  are calculated from the active impedances. Then the phase of the reflection coefficients  $\phi_n$  are determined.
3. Using standard transmission line formulas, the assumed currents at the reference planes, and the voltages determined using Eqn. 7, the voltages on the  $n$  lines are calculated when transformed in the direction away from the antenna by the phases  $\phi_n/2$ . This gives the complex voltage values at the voltage maxima (ignoring transmission line losses). The phases of these complex voltages,  $\theta_n$ , is then known. The difference between this phase and the desired phase of each current  $\theta_{targ}$  is calculated:  $\delta_n = \theta_n - \theta_{targ}$ .
4. The real powers are calculated for each line from the currents and voltages at the reference plane and summed to give the value of the total power to the antenna  $P_{tot}$ .
5. New values for the reference plane currents are calculated using the formula

$$I'_n = \sqrt{\frac{P_{targ}}{P_{tot}}} e^{-j\delta} I_n$$

where  $P_{targ}$  is the desired total power, in this case  $4 \times 25 \text{ kW} = 100 \text{ kW}$ . Note that because there is power transfer between antennas due to the mutual inductances (for relative current phases other than  $0$  or  $\pi$ ) we do not want to try to have the power on each line equal 25 kW separately, but only want the sum to be correct. The power transfer at the antennas is compensated for by the decouplers allowing equal powers to be fed from the transmitters. Thus the scaling factor the magnitude of each current is the same for each line.

6. Steps 2 through 5 are repeated until the values for  $\left| \sqrt{\frac{P_{targ}}{P_{tot}}} - 1 \right|$  and  $\delta$  reach pre-defined tolerances.

After this iteration converges,  $Z_{an}$  as well as the iterated values for the currents  $I_n$  have been determined. Iterated voltages  $V_n$  have also been determined using Eqn.3 At this point we could use standard uncoupled transmission line formulas to calculate active impedances at the load side of the decouplers, but we need the actual currents and voltages there to calculate the current through the decouplers and the impedances on the generator side of the decoupler junctions. Transmission line transformations are used to transform the currents and voltages to this location.

Then it is straightforward to determine active impedances on the generator side using

$$I_{di(i=[1,3])} = \sum_{j=[1,3]} Y_{di,j} V_j \text{ and } I_{di(i=[2,4])} = \sum_{j=[2,4]} Y_{di,j} V_j \quad (9)$$

$$I'''_n = I''_n + I_{dn} \quad (10)$$

$$V_n''' = V_n'' \quad (11)$$

$$Z_n''' = V_n''' / I_n''' \quad (12)$$

Where double primes refer to values on the load side of the decoupler network junctions, triple primes refer to values on the generator side of the decoupler network junctions, and  $n$  again refers to the lines 1 through 4.

There are two possible solutions for the parallel reactances  $X_p$  and series reactances  $X_s$  needed to match:

$$X_{p1} = \sqrt{\frac{(R_{in}^2 - Z_0 R_{in} + X_{in}^2) \frac{Z_0}{R_{in}} R_{in} + Z_0 X_{in}}{R_{in} - Z_0}} \quad (13)$$

$$X_{s1} = -\frac{(R_{in}^2 + X_{in}^2 + X_{in} X_{p1}) X_{p1}}{R_{in}^2 + X_{in}^2 + X_{p1}^2 + 2X_{in} X_{p1}} \quad (14)$$

and

$$X_{p2} = -\sqrt{\frac{(R_{in}^2 - Z_0 R_{in} + X_{in}^2) \frac{Z_0}{R_{in}} R_{in} - Z_0 X_{in}}{R_{in} - Z_0}} \quad (15)$$

$$X_{s2} = -\frac{(R_{in}^2 + X_{in}^2 + X_{in} X_{p2}) X_{p2}}{R_{in}^2 + X_{in}^2 + X_{p2}^2 + 2X_{in} X_{p2}} \quad (16)$$

Where  $R_{in} = \text{Re}(Z_n''')$ ,  $X_{in} = \text{Im}(Z_n''')$  and  $Z_0$  is the impedance that it is desired to match to ( $= 50 \Omega$ ) which is also the characteristic impedance of the feed lines.

These reactances of course have to be calculated separately for each of the four lines, using the active impedance  $Z_n'''$  for that line. Since we want to have capacitive solutions, we choose the solution that gives a negative reactance. The capacitances can then be calculated directly. In calculating them we also take into account the series inductance of the capacitors, which is assumed to be a linear function of the capacitance and is provided by the manufacturer.

At this point all values of all components in the system have been evaluated. Using the currents and voltages already calculated, it is possible to calculate currents and voltages in the remainder of the system, including for each of the capacitors.

The results of these calculations for the present antenna design are provide below. These results were used to identify suitable capacitors for the network as listed in Table 5.

The effectiveness of the decouplers was examined for the case with the highest real power transfer between current straps, which is for a relative phasing of  $90^\circ$  between axially adjacent straps. The forward power of each of the four transmitters was set to be equal, at 25 kW each. Figure 21 shows that the currents at the strap grounds are very nearly equal. The difference at 0.5 ohms loading is  $\sim 2\%$ . However, as can be seen in Figure 22, the net powers at the reference planes are very unequal, and is actually  $< 0$  for straps 2 and 4 for resistive loading  $\lesssim 0.8 \Omega$ . This means that power in these straps is actually flowing from the antenna towards the transmitters. It is redirected through the decoupler connections. Note that

for all values of resistance the sum of the powers in the four lines in Figure 22 is 100 kW. Figures 23 and b are plots of decoupler capacitance values needed to completely cancel the mutual inductance between axially adjacent straps, for respectively the cases  $f = 13.56$  MHz and  $f = 27$  MHz. These are fairly insensitive to the resistance value, and in actuality it would be possible to set them at a value optimized for the actual resistance and leave them fixed at that point. Shot-to-shot retuning of these should not be necessary. The currents and voltages in the decoupler capacitors are also fairly low. These are shown in Figure 24 for  $f = 13.56$  MHz and Figure 25 for  $f = 27$  MHz.

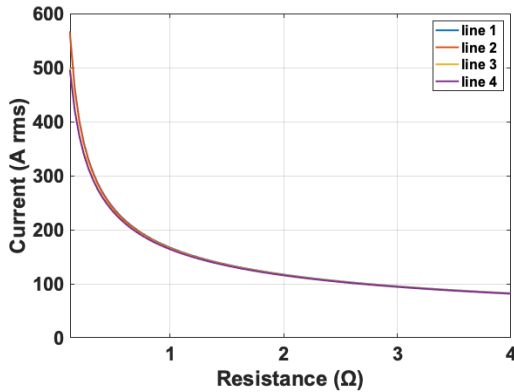


Figure 21. Strap current magnitudes vs. R for four lines with  $90^\circ$  phasing between axially adjacent straps

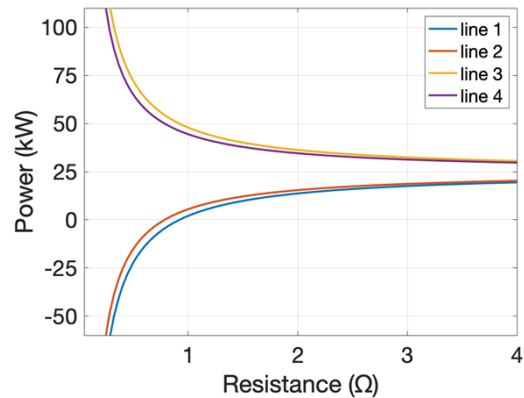
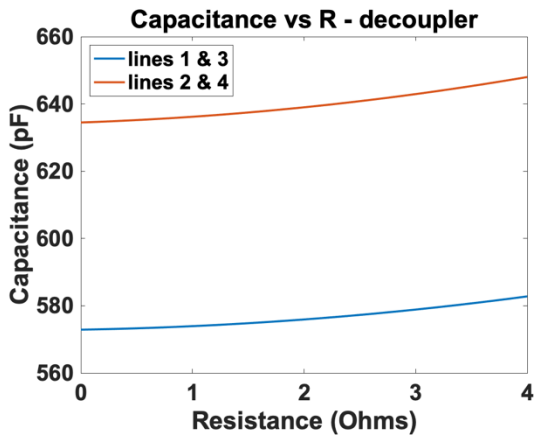
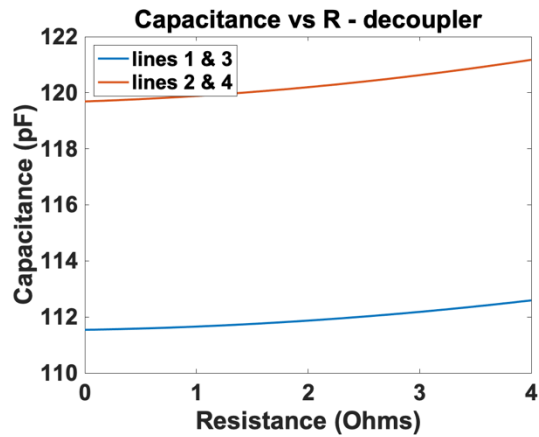


Figure 22. Net power at antenna input ports for same case as Figure 21.



a)



b)

Figure 23. Decoupler capacitances vs. R for a)  $f = 13.56$  MHz, b)  $f = 27$  MHz.

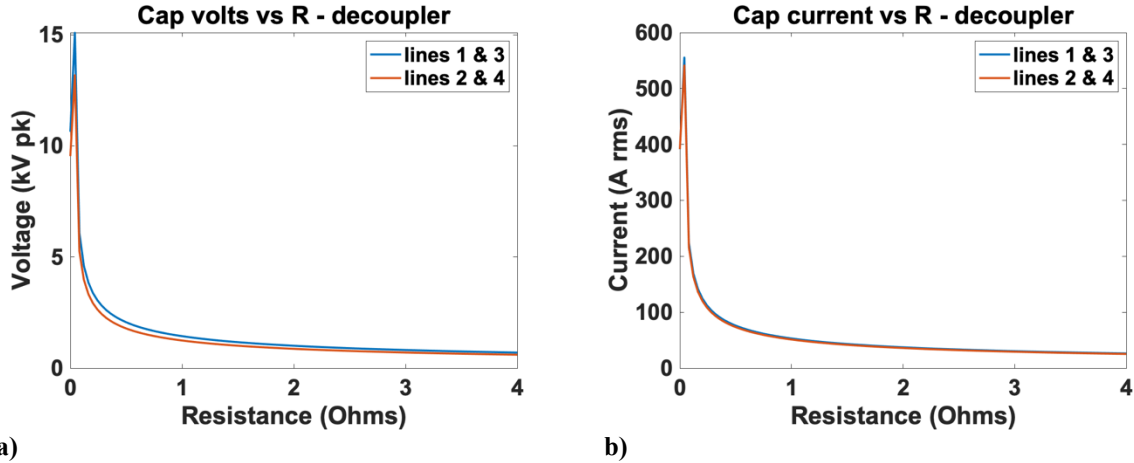


Figure 24. Decoupler capacitor a) currents, and b) voltages, for  $f = 13.56$  MHz and  $90^\circ$  phasing

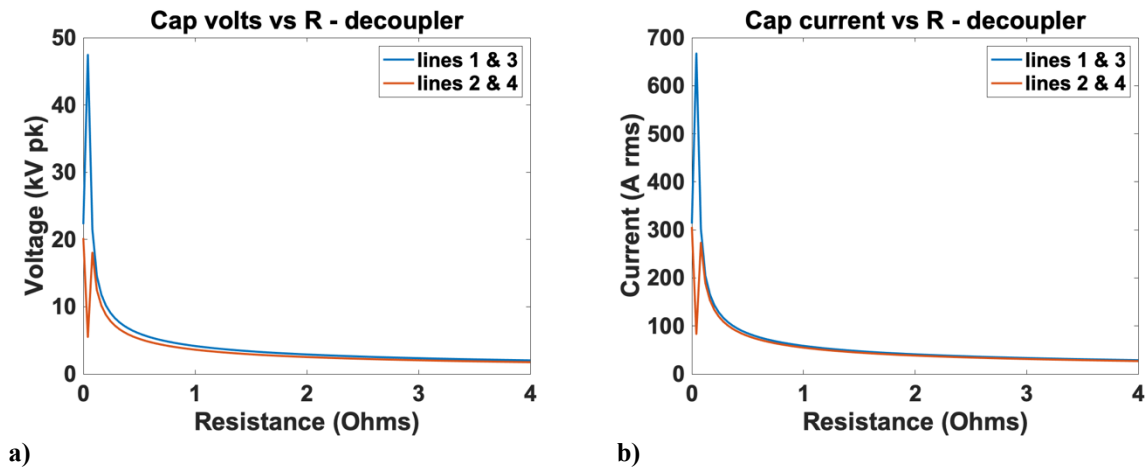


Figure 25. Decoupler capacitor a) currents, and b) voltages, for  $f = 27$  MHz and  $90^\circ$  phasing

Turning to the matching networks, the capacitances needed for an impedance match as a function of resistive loading, together with currents and voltages for all capacitors are shown in Figures 26 a-c for  $f = 13.56$  MHz. The corresponding plots for  $f = 27$  MHz are provided in Figures 27 a-c. The calculations were all performed with  $90^\circ$  phasing between axially neighboring straps, but because of the decouplers the quantities plotted do not vary much with phase.

The dashed lines in Figures 26a and 27a correspond to the capacitance limits for the selected capacitors listed in Table 5. The blue lines refer to the series and red lines to the shunt capacitors. In Figures 26 b,c and 27b,c horizontal lines correspond to capacitor current or voltage limits and vertical lines to the resistance values at these limits. The plots include both series and shunt capacitors, but in all cases the dashed lines are associated with the capacitor with the highest limiting R value. The line color indicates whether the limit is due to the series (blue) or shunt (red) capacitor.

The voltage limits are set by the manufacturer and are peak working voltages ( $U_{pw}$ ) these are conservative and are considerably below the peak test voltages ( $U_{pt}$ ) that the manufacturer tests the capacitors to. The current limits chosen are above those set by the manufacturer. This is because the manufacturer's limits correspond to CW operation, whereas the pulse length for the TAE system will be very short:  $\leq 20$  ms.



They are based on the percentage overcurrent reliably achieved for similar but not identical capacitors operated on the ORNL Proto-MPEX plasma device for pulse lengths up to 1 s with a duty factor  $\leq 0.3\%$ . Because in the case of C-2W the pulse length is  $\ll 1$  s it is likely that they could be operated at significantly higher current, resulting in a lower plasma resistance limit. An accurate assessment would require knowledge of the capacitor electrode masses in order to calculate  $\Delta T$  for these structures during a pulse.

It can be seen that capacitor current limits resistances to considerably higher values than voltage does. It would be useful in the future to obtain additional information on the capacitor structures in order to calculate more accurate limits, which would bring them closer to the limits imposed by the voltage.

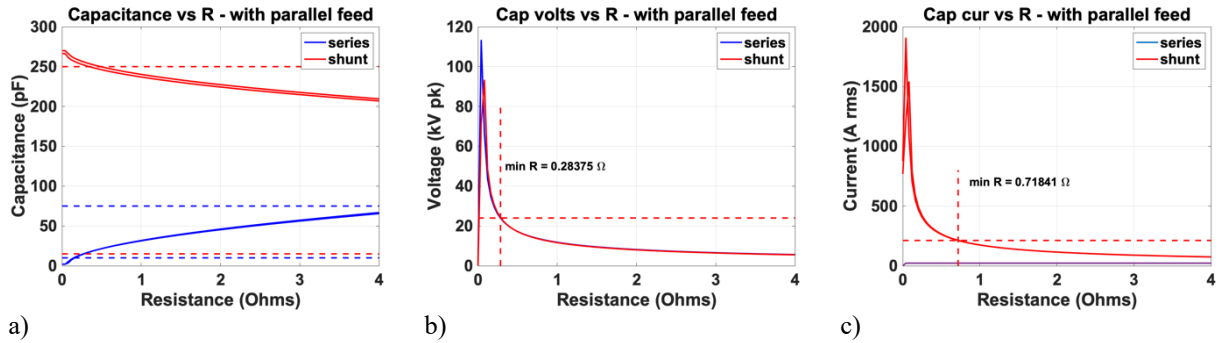


**Figure 26 a) Capacitances vs. R, b) Capacitor voltages vs. R, and c) Capacitor currents vs. R for  $f = 13.56$  MHz and  $90^\circ$  phasing**

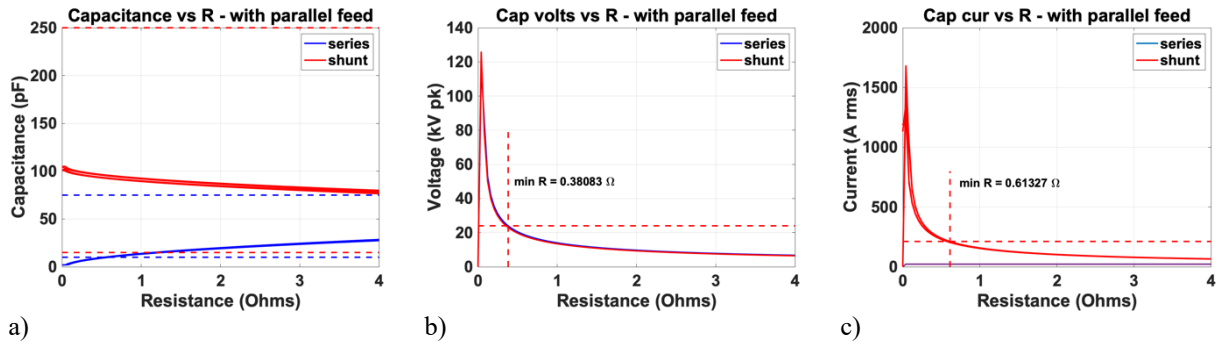


**Figure 27 a) Capacitances vs. R, b) Capacitor voltages vs. R, and c) Capacitor currents vs. R for  $f = 27$  MHz and  $90^\circ$  phasing**

### 3.2 MECHANICAL DESIGN (TAE TEAM)

The principal requirements of the mechanical design were driven by the limited port access on the C-2W machine and the large number of neutral beams (8) and neutral beam dumps (4) that had to be avoided. This required targeting a port away from the midplane. Additionally, in order to excite the fast wave, the RF power must traverse the scrape-off layer to reach the cut-off density, a distance of several cm. Since it is not precisely known how far the antenna may be inserted into the plasma without causing a disruption or suffering damage itself, nor precisely how large a distance the RF can bridge as an evanescent wave (although that distance can be accurately calculated in the ideal scenario, see below, the effect that density fluctuations may have on transmission is much harder to predict). We therefore required that the antenna

be mounted on an insertable assembly so that coupling studies can be performed. Finally, the mechanical design had to accommodate the bulky capacitors required for load matching.

The mechanical requirements can be summarized justly:

- 4 straps in either a 2x2 or 4x1 configuration
- Not located in beam footprint
- Does not require the removal of any neutral beams
- Straps curved to match plasma shape
- Insertable from the wall at  $r = 80$  cm to  $r = 70$  cm
- Capable of handling up to 50 kW per strap
- Work with ORNL RF Engineers to determine:
  - Strap width and spacing (subject to mechanical constraints of the port)
  - Electrical circuit of antenna
  - Feedthrough size and insulation
  - Accommodate Faraday shielding and boron nitride box

As a result of those requirements and iterating with the ORNL team to maintain RF fidelity, the final design was reached and is shown in Figure 28 below. The matching network shown in the electrical circuit diagram in Figure 18 is realized by in the large boxes mounted on the sides (aka “the saddlebags”).

The matching circuit for each individual strap is comprised of a series capacitor, a shunt capacitor, and a decoupling inductor and capacitor. The circuits of each azimuthal pair share a box (i.e., one circuit per strap, two circuits per box). It can also be seen in Figure 28 that the capacitances of the series and shunt capacitors can be adjusted remotely with servo motors mounted on the tops and bottoms of the boxes. The capacitances of the decoupling capacitors will be only manually adjustable.

The entire assembly, including matching networks is translatable. In Figure 28 a, the antenna is inserted to its maximum depth. In the retracted position, the front of the Faraday cage is flush with the vessel wall.

Armed with the  $k_{\parallel}$  spectra shown in Figure 12, we can combine the measured C-2W equilibrium density profile and the expression for the cut-off density to obtain the coupled power as a function of antenna insertion depth for the two generator frequencies under consideration. The results are plotted in Figure 29. We can reasonably expect to be able to insert the antenna to  $r=73$  cm. At 27 MHz, this would result in about 60% of the power radiated from the antenna reaching the plasma, more than enough for proof-of-concept experiments

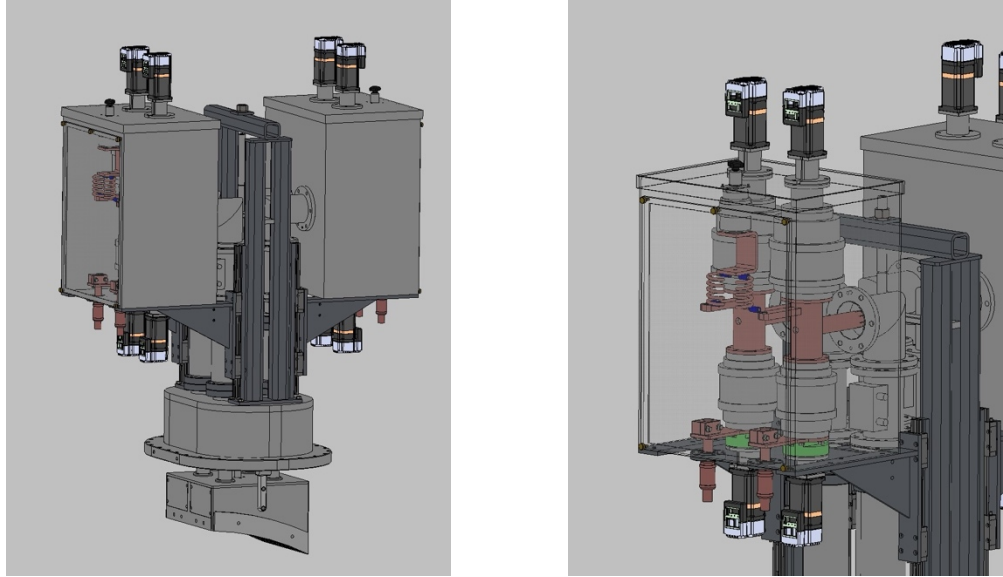


**Figure 28 a) CAD model of the HHFW antenna assembly shown in the inserted position b) Cut-away showing matching network.**

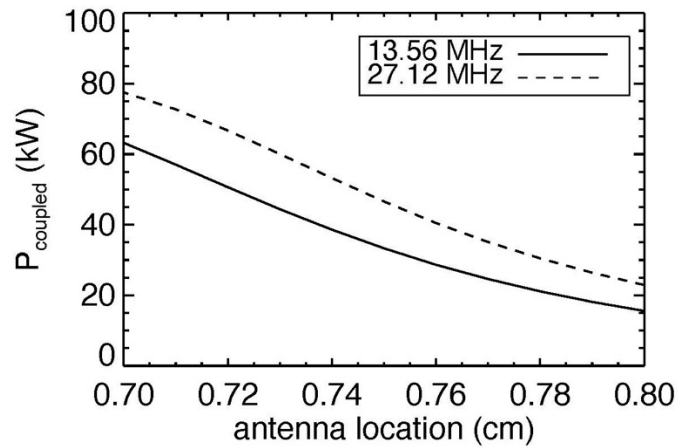


**Figure 29. 1D calculation of power delivered to plasma across evanescent region as a function of antenna insertion depth for both  $f=13.56$  and  $f=27.12$  MHz, assuming 100 kW of rf power launched.**

#### 4. COMMERCIALIZATION POSSIBILITIES

No commercialization possibilities beyond the potential fusion-enabling RF plasma heating technology described above were identified during the course of this work.

## 5. PLANS FOR FUTURE COLLABORATION

The ultimate goal of TAE's RF program is the installation of a high power RF heating system on its next generation FRC device, Copernicus. The completion of the project described above represents significant progress towards that goal, but much work remains. For the next step, ORNL and TAE have submitted a new INFUSE proposal as part of the 2024a call to integrate the finite element edge physics model RAPLICA-SOL with TAE's in-house RF simulation package, RFPisa, so that the problem can be simulated with edge physics and global mode excitation fully integrated. This work described above will allow the integrated simulation to be benchmarked against experimental data.

## 6. CONCLUSION

The successful completion of the project described above has delivered a mature and complete design, in both the mechanical and electrical engineering sense, of a robust and flexible HHFW antenna for the C-2W machine.

The design is practical, optimized for ease of assembly and integration. The antenna can deliver up to 200 kW to the plasma (50 kW per strap) in a 2 azimuthal x 2 axial arrangement, although the intent for first experiments and the calculations shown here pertain to 100 kW total. The electrical response has been evaluated for both  $f=13.56$  MHz and  $f=27.12$  MHz, and both can be accommodated with minimal changes to the electrical circuitry of the matching networks, providing flexibility in the ultimate choice of generator.

Two of the key engineering solutions were driven by the principal physics questions to be answered of how big an evanescent gap can be bridged in the presence of edge density fluctuations, and how can that bridging be accomplished without disrupting the plasma? First, the straps are decoupled so that they may be individually phased to explore the relationship between phasing and plasma coupling. Calculations indicate that small antenna strap phasing can reduce  $k_{\parallel}$  and thus, the cut-off density, improving overall coupling. Second, the entire assembly is translatable over 10 cm, so the location of wave launched can be varied.

The lessons learned from this experiment will be of interest to the wider fusion community and allow TAE to move to the next phase of its research program, constructing a MW-class system for heating of its next generation FRC.

## REFERENCES

- [1] M. W. Binderbauer *et al.*, "A high performance field-reversed configuration," *Phys. Plasmas*, vol. 22, no. 5, p. 056110, May 2015, doi: 10.1063/1.4920950.
- [2] H. Gota *et al.*, "Formation of hot, stable, long-lived field-reversed configuration plasmas on the C-2W device," *Nucl. Fusion*, vol. 59, no. 11, p. 112009, Nov. 2019, doi: 10.1088/1741-4326/ab0be9.
- [3] H. Gota *et al.*, "Overview of C-2W: high temperature, steady-state beam-driven field-reversed configuration plasmas," *Nucl. Fusion*, vol. 61, no. 10, p. 106039, Oct. 2021, doi: 10.1088/1741-4326/ac2521.
- [4] S. V. Putvinski, D. D. Ryutov, and P. N. Yushmanov, "Fusion reactivity of the pB<sup>11</sup> plasma revisited," *Nucl. Fusion*, vol. 59, no. 7, p. 076018, Jul. 2019, doi: 10.1088/1741-4326/ab1a60.
- [5] X. Yang *et al.*, "Overview of TAE technologies' HHFW project on LAPD," in *AIP Conference Proceedings*, Hefei, China, 2020, p. 070002. doi: 10.1063/5.0013563.

- [6] X. Yang *et al.*, “Simulations of High Harmonic Fast Wave Heating on the C-2U Advanced Beam-Driven Field-Reversed Configuration Device,” *EPJ Web Conf.*, vol. 157, p. 03065, 2017, doi: 10.1051/epjconf/201715703065.
- [7] Hill, D. N., “Report of the FESAC Toroidal Alternates Panel,” DOE, Washington, D.C., Nov. 2008.
- [8] Hazeltine, R., “Research Needs for Magnetic Fusion Energy Sciences,” Bethesda, Maryland, Jun. 2009.
- [9] N. J. Fisch, “The Alpha Channeling Effect,” AIP Conference Proceedings 1689, 020001 (2015); doi: 10.1063/1.4936463
- [10] E.D. Fredrickson, et al., “Suppression of energetic particle driven instabilities with HHFW heating,” *Nucl. Fusion* 55 (2015) 013012
- [11] D. Liu, et al., “Profiles of fast ions that are accelerated by high harmonic fast waves in the National Spherical Torus Experiment,” *Plasma Phys. Control. Fusion* 52 (2010) 025006
- [12] W. Tierens, R. Bilato, N. Bertelli, S. Shiraiwa, J. Myra, and L. Colas, “On the origin of high harmonic fast wave edge losses in NSTX,” *Nucl. Fusion*, vol. 62, no. 9, p. 096011, Sep. 2022, doi: 10.1088/1741-4326/ac7c7d.
- [13] R. J. Perkins et al., “High-Harmonic Fast-Wave Power Flow along Magnetic Field Lines in the Scrape-Off Layer of NSTX,” *Phys. Rev. Lett.*, vol. 109, no. 4, p. 045001, Jul. 2012, doi: 10.1103/PhysRevLett.109.045001.
- [14] <https://hamwaves.com/qoil/>

Final Report Certification  
for  
CRADA Number \_\_\_\_\_

Between

UT-Battelle, LLC

and

TAE Technologies, Inc  
(Participant)

**Instructions:**

Mark the appropriate statement in 1a or 1b below with an 'X.' Refer to the articles in the CRADA terms and conditions governing the identification and marking of Protected CRADA Information (PCI).

If no PCI is identified, the report will be distributed without restriction. If PCI is identified, the report distribution will be limited in accordance with the CRADA terms and conditions governing release of data. In all cases items 2 and 3 must be true. That is, the report cannot contain Proprietary Information and a disclosure must be filed prior to release of the report.

This certification may either be made by using this form or may be made on company letterhead if the Participant desires. A faxed copy of this completed form is acceptable.

The following certification is made for the subject final report:

1. (a)  The final report contains information that qualifies as "Protected CRADA Information" (PCI). The PCI legend is printed on the report cover, and the PCI is clearly identified.


OR

(b)  The final report does not contain "Protected CRADA Information." The "Approved for Public Release" legend is printed on the report cover.

2. The final report does not contain Proprietary Information.

3. By the signature below, the Participant has no objection to the public distribution of the final report due to patentable information.

For the Participant:

Artem Smisnov   
(Name)

CTO  
(Title)

04/18/2024  
(Date)